electronics

MDPI

Article

Near-to-Far Field RCS Calculation Using Correction Optimization Technique

Jinhai Huang [1,2], Jianjiang Zhou [1,*] and Yao Deng [1]

[1] Key Laboratory of Radar Imaging and Microwave Photonics, Nanjing University of Aeronautics and Astronautics, Nanjing 210016, China; jinhaiwell@nuaa.edu.cn (J.H.); dy111896@nuaa.edu.cn (Y.D.)
[2] College of Electronic Engineering, Guilin Institute of Information Technology, Guilin 541004, China
* Correspondence: zjjee@nuaa.edu.cn

Abstract: Radar cross section (RCS) is a scattering measure of an object that scatters to the radar. However, existing methods for near-field (NF) measurement and data processing rarely extract amplitude characteristics, and there is a lack of effective verification of far-field (FF) data in the process of NF to FF transformation, which leads to inaccuracies in FF prediction accuracy. In this paper, we propose a method to establish the relationship between the NF and FF RCS using the state space method (SSM), which is based on accurate estimation of the NF amplitude in NF measurement, and then deriving the FF RCS from the NF scattering signal convolved with a near-to-far kernel. The proposed solution to address the uncertainty issue in reference FF data involves using the geometric theory of diffraction (GTD) scattering center model as the reference FF data and establishing a linear equation with the derived FF model. The negative gradient search (NGS) system identification concept is used to optimize the FF model in order to reduce the discrepancy between the reference and derived values. Finally, the corrected RCS error is provided as additional proof of the effectiveness of these techniques in enhancing near-to-far transformation accuracy by examining the outcomes of three experiments.

Keywords: radar cross section (RCS); near-to-far transformation; dyadic Green's function; state space method (SSM); geometry theory of diffraction (GTD); negative gradient search (NGS); system identification

Citation: Huang, J.; Zhou, J.; Deng, Y. Near-to-Far Field RCS Calculation Using Correction Optimization Technique. *Electronics* **2023**, *12*, 2711. https://doi.org/10.3390/electronics12122711

Academic Editor: Massimiliano Pieraccini

Received: 24 April 2023
Revised: 11 June 2023
Accepted: 14 June 2023
Published: 17 June 2023

1. Introduction

1.1. Background and Motivation

The RCS parameter serves not only as a key metric for evaluating the stealth performance of a target, but also as a vital characteristic parameter that reflects the target's electromagnetic (EM) properties. Nevertheless, the requisite FF instrumentation for measuring this parameter can prove to be both costly and difficult to obtain. To overcome this challenge, engineers frequently employ the near-to-far transformation technique, which extrapolates the FF RCS from NF measurement data. The precise reconstruction of RCS necessitates a complete set of fragmented scattering data. However, this requirement may prove unattainable due to the unavailability of data or time constraints in certain scenarios. In response, numerous algorithms have been developed to predict RCS from single-station NF measurements, which are commonly recognized as prediction, extrapolation, or extraction techniques [1]. Although these approaches entail certain approximations, they have been effectively implemented in practical applications, and in several instances, have yielded accurate results.

In [2], the authors introduce the reflectivity distribution image method, a widely used approach in synthetic aperture radar (SAR) imaging for estimating the reflectance of a target from the radar signal measured. Even though the method does not explicitly compute an image, its algorithms are commonly referred to as image-based techniques. However,

the method has certain limitations, notably the absence of explicit treatment of multiple scattering effects. Instead, these effects are accounted for by a single scattering contribution from the virtual target that varies with the measured distance, which can be challenging when predicting RCS from NF observations.

Due to the typically electrically large scattering objects, numerous algorithms for predicting RCS rely on the periodic sampling of NF data obtained using conventional acquisition geometries, such as planar, cylindrical, or spherical [3] shapes. However, current algorithms demand a rigorous specification of the position and polarization modes for NF measurements. For instance, the full wave acceleration algorithm based on fast Fourier transform (FFT) must integrate the target using a sampling grid. Most methods for modeling all polarization effects are based on scalar formulas, where each polarization can be horizontal, vertical, or intersecting. Consequently, most prediction algorithms require specific NF measurement and data processing techniques, which may limit the accuracy of predictions if certain characteristic parameters, such as amplitude and phase, are not properly extracted.

In [4], the authors have presented a novel approach to estimate the FF uncertainty using the fast irregular antenna field transformation algorithm, which can be utilized in planar, cylindrical, and spherical NF measurements, as well as arbitrary measurement grids. However, the article lacks a clear explanation regarding the procedure for acquiring reference FF data. The authors have simply assumed the availability of such data and employed it as a standard to evaluate the NF measurement outcomes. Hence, the prediction of FF RCS accuracy remains uncertain.

In this paper, we concentrate on the establishment of the RCS relationship between the NF and FF based on the SSM used in NF measurement to accurately estimate the NF amplitude and derive the FF RCS. To address the uncertainty issue in reference FF data, a GTD scattering center model can be considered as the corresponding reference FF data and a linear equation is established with the derived FF model. To reduce the error between the reference and derived values, the FF model is optimized using the NGS system identifying principle.

1.2. Main Contribution

The following is a summary of this article's significant contributions.

(1) The transformation operator from the transmitter to the receiver in the Cartesian coordinate system of free space is calculated using the dyadic Green's function. The amplitude estimation problem of NF-receivedd signals is addressed using the SSM.

(2) The derivation of the near-to-far transformation kernel is constructed, and the equation for transforming NF signals to FF is established, solving the RCS calculation for FF signals.

(3) A GTD model for EM scattering is built using the spatial distance vector corresponding to the FF response. The relationship equation between the FF signal composed of the near-to-far transformation kernel and the GTD-FF signal model is established, serving as the predictive model for FF measurement data.

(4) The scattering signals derived from the near-to-far transformation kernel and the average values obtained from the GTD model are calculated. A system identification model is established to estimate the correction coefficient vector, addressing the issue of large RCS errors in the FF.

The subsequent sections will introduce the theory of the NF model, NF amplitude estimation, near-to-far transformation, and FF NGS system identification correction optimization method for RCS, which is detailed in Section 2. Section 3 provides a concise overview of the near-to-far transformation numerical simulation for RCS analysis. Finally, Section 4 presents our conclusions.

2. Methods

Accurate measurement of RCS requires the acquisition of radar data. NF RCS measurements can be obtained through monostatic radar measurements, which enable the prediction of the RCS of unknown scattering objects. To achieve accurate results, it is necessary to use an appropriate conversion algorithm that takes into account the arbitrary target measurement position and antenna direction. Moreover, the sampling requirements must be met to ensure the accuracy of the RCS measurements.

To accurately model the scattering behavior in the NF, the authors in [5] utilize a radiation reflector model and a multilevel plane wave decomposition method. In particular, the incident waves are decomposed into a series of plane waves with varying frequencies and directions, whereas the scattering waves are modeled as though they originate from a set of reflectors.

The model's method comprises the following four steps:

(1) A hierarchy of known or anticipated scattering center shapes is used to symbolize the item.

(2) Develop a model to show the connection between the incident wave and the spread wave.

(3) To determine the RCS, a series of linear equations must be computed.

(4) Determine the object's RCS using the response from Step 3 as a starting point.

2.1. NF Scattering Model and Amplitude Estimation

2.1.1. NF Scattering Model

As illustrated in Figure 1, a reference coordinate system (x, y, z) is provided to describe the interaction between the antenna under test (AUT) and an unspecified test target surface. The distance vectors from the transmitting and receiving antennas to the target phase reference center are denoted as $\boldsymbol{r}$ and $\boldsymbol{r}'$, respectively, and the position of the scattering point in this reference coordinate system is represented by $\boldsymbol{r}_i$. When considering a monostatic case, $\boldsymbol{r}$ is equal to $\boldsymbol{r}'$. It should be noted that each scattering point has its own propagation vector k_i directed towards the center of the associated facets, which can be viewed as a separate incident field E_i. Therefore, the spatial three-dimensional distance vector between the target reference coordinate origin and the transmitting antenna can be written as

$$\boldsymbol{r} = x\hat{\boldsymbol{x}} + y\hat{\boldsymbol{y}} + z\hat{\boldsymbol{z}} \tag{1}$$

where $(\hat{\boldsymbol{x}}, \hat{\boldsymbol{y}}, \hat{\boldsymbol{z}})$ is the unit vector along (*x*,*y*,*z*) directions, respectively. The complex EM transmission system can be approximated using a linearized forward operator, wherein the input signal can be represented as a complex waveform or spectrum. This approach enables the capture of the relationship between input and output variables, as depicted in Figure 1. It is assumed within this approach that small perturbations in the input variables result in proportional changes in the output variables. In this case, the equivalent current density distribution $\boldsymbol{J}_s$ in free space represents the radar antenna in transmit mode. This distribution can be normalized with respect to the excitation voltage $\boldsymbol{U}_{in}$ at the antenna feed port, resulting in

$$\boldsymbol{J}_s(\boldsymbol{r}) = \boldsymbol{U}_{in}(\boldsymbol{r})\mathrm{w}_T(\boldsymbol{r}) \tag{2}$$

where w_T is a weighting function for transmitting impedance that depends on the reference coordinate system, $\boldsymbol{Gn}(\boldsymbol{r}_i, \boldsymbol{r})$ is the dyadic Green's function in free space, and $\boldsymbol{J}_s$ is the current distribution that generates the incident field $\boldsymbol{E}^i(\boldsymbol{r})$ at the scatterer

$$\boldsymbol{E}^i(\boldsymbol{r}) = -\frac{jkZ_F}{4\pi} \iiint_V \boldsymbol{Gn}(\boldsymbol{r}_i, \boldsymbol{r})\boldsymbol{J}_s(\boldsymbol{r})d^3\boldsymbol{r} \tag{3}$$

$$\boldsymbol{Gn}(\boldsymbol{r}_i, \boldsymbol{r}) = \left(\bar{\mathbf{I}} + \frac{1}{k^2}\nabla\nabla\right)\frac{\exp(-j\boldsymbol{k}\|\boldsymbol{r}_i - \boldsymbol{r}\|)}{\|\boldsymbol{r}_i - \boldsymbol{r}\|} \tag{4}$$

where V in (3) is determined by the spatial extent of the scatterer, Z_F represents the characteristic impedance of free space, k in (3) is the scalar of wave number, $\boldsymbol{k} = k_x\hat{k}_x + k_y\hat{k}_y + k_z\hat{k}_z$ in (4) is the vector of wave number, ∇ is the gradient operator, $\bar{\mathbf{I}} = \hat{x}\hat{x} + \hat{y}\hat{y} + \hat{z}\hat{z}$ is the unit dyad, and $\|\boldsymbol{r}_i - \boldsymbol{r}\|$ represents the norm of distance vector between the target and transmitting AUT. Similarly, the dyadic Green's function for the free space of the receiving field can be written as

$$\boldsymbol{Gn}'(\boldsymbol{r}_i, \boldsymbol{r}') = \left(\bar{\mathbf{I}} + \frac{1}{k^2}\nabla\nabla\right)\frac{\exp(-j\boldsymbol{k}\|\boldsymbol{r}_i - \boldsymbol{r}'\|)}{\|\boldsymbol{r}_i - \boldsymbol{r}'\|} \tag{5}$$

where $\boldsymbol{r}'$ is the distance vector in the space domain between the reference source point and the receiving antenna. To shift the phase reference center of the target scattering function from the radar receiving antenna to the center of the target, it is necessary to introduce a phase term into the NF scattered field. The scattered signal from the NF to the receiving antenna can then be obtained as

$$\boldsymbol{E}^s(\boldsymbol{r}') = \iiint_V \alpha_i \boldsymbol{Gn}'(\boldsymbol{r}_i, \boldsymbol{r}')\boldsymbol{E}^i(\boldsymbol{r})\exp(-j\boldsymbol{k}\cdot\boldsymbol{r}')d^3\boldsymbol{r}' \tag{6}$$

where α_i is the i-th magnitude coefficient to be estimated. The Born approximation [6], which assumes negligible interaction between the antenna and the scatterer, establishes a linear relationship between the scattered fields and is used to model the scattering behavior in radar imaging. This approach is preferred over a nonlinear formulation. In addition, based on the principle of reciprocity, the weighting function for the receiving antenna, denoted as w_R, is defined identically to the weighting function for the transmitting antenna, denoted as w_T. When the voltage U_m [1] is measured at the receiving port, it can be derived as follows:

$$\begin{aligned} U_m &= \iiint_V \mathrm{w}_R(\boldsymbol{r}')\boldsymbol{E}^s(\boldsymbol{r}')d^3\boldsymbol{r}' \\ &= \iiint_V \iiint_V \alpha_i \mathrm{w}_T(\boldsymbol{r})\boldsymbol{Gn}'(\boldsymbol{r}_i, \boldsymbol{r}')\boldsymbol{E}^i(\boldsymbol{r})\exp(-j\boldsymbol{k}\cdot\boldsymbol{r}')d^3\boldsymbol{r}'d^3\boldsymbol{r}' \\ &= -\frac{jkZ_F}{4\pi}\iiint_V \iiint_V \iiint_V \alpha_i \mathrm{w}_T(\boldsymbol{r})\boldsymbol{Gn}'(\boldsymbol{r}_i, \boldsymbol{r}')\boldsymbol{Gn}(\boldsymbol{r}_i, \boldsymbol{r})\boldsymbol{J}_s(\boldsymbol{r})\exp(-j\boldsymbol{k}\cdot\boldsymbol{r}')d^3\boldsymbol{r}'d^3\boldsymbol{r}'d^3\boldsymbol{r} \end{aligned} \tag{7}$$

where the triple integral of V with respect to its limits represents the calculation performed by the monostatic system, hence resulting in the equality of w_R and w_T.

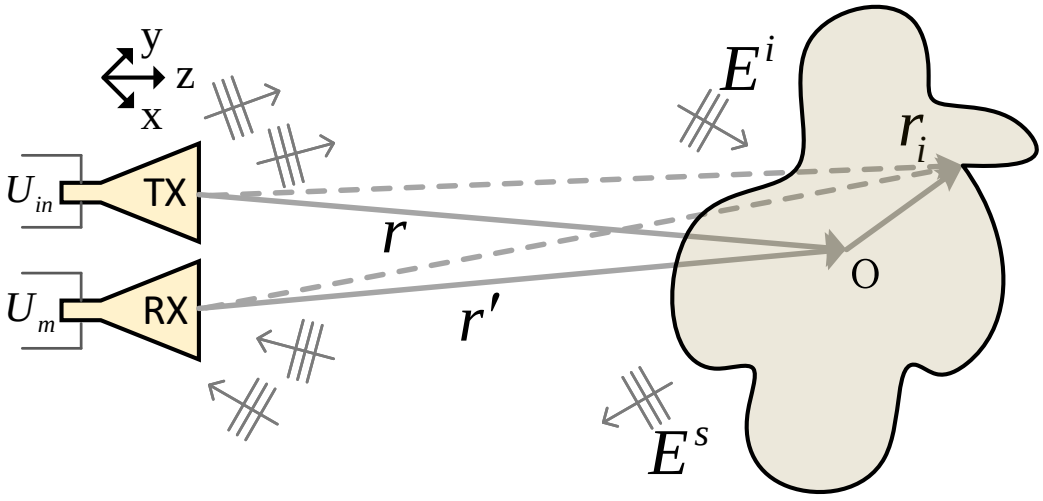

Figure 1. The structure of NF antenna for test target.

In engineering applications, discrepancies often arise between the theoretically predicted and actual measured values of the receiving field voltage. Neglecting this error can lead to unpredictable deviations in subsequent calculations, making error correction necessary.

2.1.2. Amplitude Estimation

The state space Equation [7] is established based on the scattered field signal and a sample of measured voltage parameters, given by

$$\begin{aligned} E^i(k+1) &= AE^i(k) + Bu(k) \\ E^s(k) &= CE^i(k) + u(k) \end{aligned} \tag{8}$$

where $E^i(k)$ and $E^s(k)$ are k-th component of $\boldsymbol{E}^i(\boldsymbol{r})$ and $\boldsymbol{E}^s(\boldsymbol{r}')$, respectively. $A \in C^{M\times M}$ is the open-loop matrix, $B \in C^{M\times 1}$, $C \in C^{1\times M}$ are constant matrices. Then, proceeding by constructing the Hankel matrix from Equation (8)

$$\mathbf{H} = \begin{bmatrix} \frac{E^s(1)}{U_m} & \frac{E^s(2)}{U_m} & \cdots & \frac{E^s(L)}{U_m} \\ \frac{E^s(2)}{U_m} & \frac{E^s(3)}{U_m} & \cdots & \frac{E^s(L+1)}{U_m} \\ \vdots & \vdots & \vdots & \vdots \\ \frac{E^s(N-L+1)}{U_m} & \frac{E^s(N-L+2)}{U_m} & \cdots & \frac{E^s(N)}{U_m} \end{bmatrix} \tag{9}$$

where $E^s(N)$ is the component of $\boldsymbol{E}^s(\boldsymbol{r}')$, L stands for the correlation window's length and N is heuristically set to [L/2], and the value in brackets represents the lowest integer that is less than or equal to the inserted value. The eigen-structure of Hankel matrices is utilized by subspace decomposition techniques to estimate the parameters of linear time-invariant(LTI) signal models [8]. In light of this, we compute the singular value decomposition (SVD) of the H matrix and perform low-rank truncation to extract the relevant signal components, it leads to the following equation:

$$\tilde{\mathbf{H}} = \mathbf{U}_{sn}\mathbf{\Sigma}_{sn}\mathbf{V}_{sn}^*. \tag{10}$$

In Equation (10), the noise-corrupted signal component is denoted by the subscript $'sn'$. $\mathbf{U}_{sn}$ represents the left-unitary matrix, whereas $\mathbf{\Sigma}_{sn}$ is a diagonal matrix consisting of the singular values of $\mathbf{H}$. The right-unitary matrix's conjugate transpose is represented by $\mathbf{V}_{sn}^*$. Furthermore, it is possible to further factorize the Hankel matrix by using the balanced coordinate transformation [9].

$$\tilde{\mathbf{H}} = \tilde{\mathbf{\Omega}}\tilde{\mathbf{\Gamma}} \tag{11}$$

where $\tilde{\mathbf{\Omega}} = \mathbf{U}_{sn}\mathbf{\Sigma}_{sn}^{1/2}$ refers to the finite-rank observability matrix, and $\tilde{\mathbf{\Gamma}} = \mathbf{\Sigma}_{sn}^{1/2}\mathbf{V}_{sn}^*$ refers to the controllability matrix. Then, the open-loop matrix $\mathbf{A} \in C^{M\times M}$ can be derived by the observability matrix $\tilde{\mathbf{\Omega}}$

$$\mathbf{A} = \left(\tilde{\mathbf{\Omega}}_{-r\ell}^*\tilde{\mathbf{\Omega}}_{-r\ell}\right)^{-1}\tilde{\mathbf{\Omega}}_{-r\ell}^*\tilde{\mathbf{\Omega}}_{-r1} \tag{12}$$

where the matrices $\tilde{\mathbf{\Omega}}_{-r\ell}$ and $\tilde{\mathbf{\Omega}}_{-r1}$ in Equation (11), respectively, are removing the final and first rows of $\tilde{\mathbf{\Omega}}$. Furthermore, the eigenvalue of $\mathbf{A}$ can be calculated as

$$\lambda\{\mathbf{A}\} = \{\lambda_1, \lambda_2, \cdots, \lambda_M\} \tag{13}$$

For use in engineering involving linear transformations or LTI systems, a set of input vectors is typically matched with a set of output vectors. The appropriate eigenvalue can be considered as the gain of the linear system input, where each input vector is treated as the input to an LTI system. Signal amplitude estimation can be obtained by applying Equation (13) and representing the eigenvalue as its gain.

$$\alpha_i = -\frac{\log|\lambda_i|}{\Delta\varphi} \tag{14}$$

where $\Delta\varphi$ is the step angle of EM wave radiation to the azimuth of the target.

As an example, Figure 2 presents a comparison among three approaches, namely SSM, TLS-ESPRIT (total least square estimation of signal parameters via rotational invariance techniques) [10], and MUSIC (multiple signal classification) [11], for parameter extraction from the geometry theory of diffraction (GTD) [12] scattering signal. The main focus of this section lies in the extraction of the scattering signal's amplitude, as higher extraction accuracy contributes to more precise calibration calculations. The simulated scattering signal is based on the GTD model defined by Equation (1) in reference [12]. The SSM method discussed in this section is employed to extract the amplitude of the signal. Additionally, the effectiveness of SSM is evaluated by comparing it with the two traditional extraction methods, TLS-ESPRIT and MUSIC. In terms of fundamental research [13], the results indicate that the SSM approach exhibits superior performance in estimating the amplitude of the GTD scattered signal at the same signal-to-noise ratio, as evidenced by the lower root mean square error (RMSE). This conclusion is drawn based on 100 Monte Carlo simulations conducted to estimate the amplitude of the GTD scattered signal and determine the RMSE.

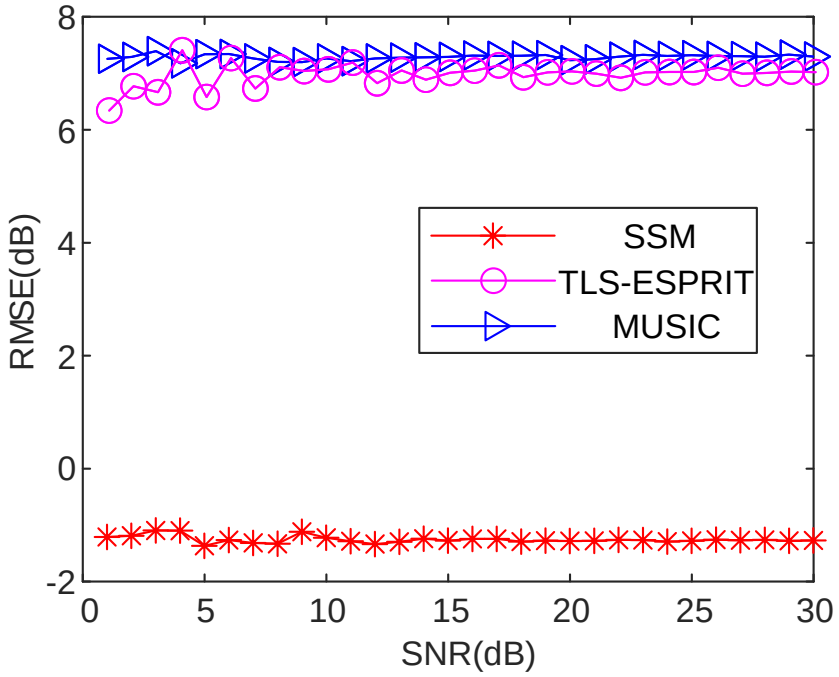

Figure 2. The comparison of the amplitude estimation method.

To validate the theoretical effectiveness of the SSM method for extracting the amplitude parameters of NF scattering E-fields, the calculation can be performed following the steps outlined below

Step 1: Initialize the NF parameters;
Step 2: Compute the equivalent current density distribution function $\boldsymbol{J}_s$;
Step 3: Calculate the NF incident E-field $\boldsymbol{E}^i(\boldsymbol{r})$;
Step 4: Compute the NF scattered E-field $\boldsymbol{E}^s(\boldsymbol{r}')$;
Step 5: Extract the amplitude parameters α_i using SSM;
Step 6: Calculate the NF-improved RCS and compare it with the reference RCS.

In contrast, Figure 3 presents a comparison of the original RCS curve of the point source target, depicted in red, with the amplitude acquired from the NF measurement using the SSM approach, represented by the blue curve. The NF RCS [14] can be computed by

$$\sigma_{NF} = \lim_{r\to\infty} 4\pi r^2 \frac{\left|\boldsymbol{E}^s(\boldsymbol{r}')\right|^2}{\left|\boldsymbol{E}^i(\boldsymbol{r})\right|^2} \tag{15}$$

where r is the distance between the antenna and the target.

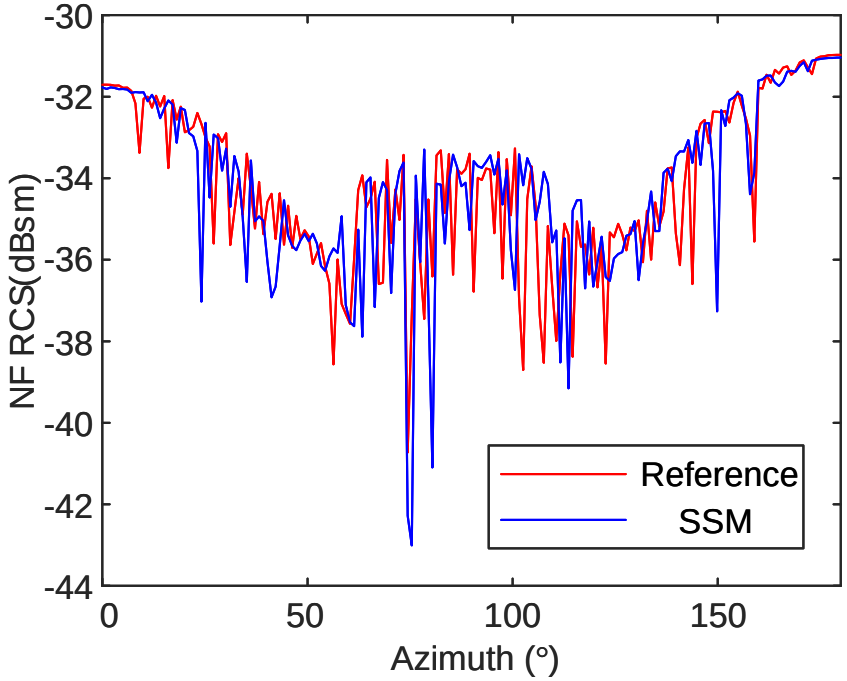

Figure 3. The comparison of NF RCS.

2.2. Near-to-Far Transformation

The acquisition of FF scattering data requires complex processing of the radiation field at each angle. In this study, the FF distance vector is defined as $\boldsymbol{r}_{FF}$ and the convolution kernel $\boldsymbol{W}(\boldsymbol{r}_{FF})$ function of the FF transform is convolved with the NF scattering signal for all transmission and reception angles. The scattering signal of the FF E-field can then be expressed as [15]

$$\boldsymbol{E}(\boldsymbol{r}_{FF}) = \boldsymbol{E}^s(\boldsymbol{r}') \otimes \boldsymbol{W}(\boldsymbol{r}_{FF}) \tag{16}$$

where the sign '$\otimes$' denotes convolution. Similarly, to relocate the phase reference center of the target scattering function from the radar receiving antenna to the target center, the scattering equation with a phase term for the FF of a plane wave can be derived as

$$\boldsymbol{E}(r_{FF}) = \iiint_V \alpha_i \boldsymbol{Gn}(\boldsymbol{r}_{FF_i}, \boldsymbol{r}_{FF}) \boldsymbol{E}^i(\boldsymbol{r}_{FF}) \exp(-j\boldsymbol{k} \cdot \boldsymbol{r}_{FF}) d^3\boldsymbol{r}_{FF} \tag{17}$$

where $\boldsymbol{r}_{FF_i}$ denotes the i-th coordinate vector of FF, the amplitude α_i can be derived from inverse Fourier Transform (IFT) of Equation (6) as follows:

$$\alpha_i = \frac{F^{-1}[\boldsymbol{E}^s(\boldsymbol{r}')]}{\boldsymbol{Gn}'(\boldsymbol{r}_i, \boldsymbol{r}')\boldsymbol{E}^i(\boldsymbol{r})}. \tag{18}$$

The FF incident E-field for the target can be obtained by the FF dyadic Green function $\boldsymbol{Gn}(\boldsymbol{r}_{FF_i}, \boldsymbol{r}_{FF})$ as

$$\boldsymbol{E}^i(r_{FF}) = -\frac{jkZ_F}{4\pi} \iiint_V \boldsymbol{Gn}(\boldsymbol{r}_{FF_i}, \boldsymbol{r}_{FF}) \boldsymbol{J}_s(\boldsymbol{r}_{FF}) d^3\boldsymbol{r}_{FF}. \tag{19}$$

By substituting Equation (18) into the FF scattering Equation (17), the resulting equation is obtained as

$$\begin{aligned} \boldsymbol{E}(r_{FF}) &= F\left[\frac{F^{-1}[\boldsymbol{E}^s(\boldsymbol{r}')]}{\boldsymbol{Gn}'(\boldsymbol{r}_i,\boldsymbol{r}')\boldsymbol{E}_i(\boldsymbol{r})}\boldsymbol{Gn}(\boldsymbol{r}_{FF_i},\boldsymbol{r}_{FF})\boldsymbol{E}^i(\boldsymbol{r}_{FF})\right] \\ &= F\left[\frac{\boldsymbol{Gn}(\boldsymbol{r}_{FF_i},\boldsymbol{r}_{FF})\boldsymbol{E}^i(\boldsymbol{r}_{FF})}{\boldsymbol{Gn}'(\boldsymbol{r}_i,\boldsymbol{r}')\boldsymbol{E}^i(\boldsymbol{r})}F^{-1}\left[\boldsymbol{E}^s(\boldsymbol{r}')\right]\right] \\ &= F\left[\omega_i F^{-1}\left[\boldsymbol{E}^s(\boldsymbol{r}')\right]\right] \end{aligned} \tag{20}$$

where $F[\cdot]$ represents the Fourier transform (FT). Consequently, ω_i is defined as the ratio of NF-to-FF, leading to

$$\omega_i = \frac{\boldsymbol{Gn}(\boldsymbol{r}_{FF_i},\boldsymbol{r}_{FF})\boldsymbol{E}^i(\boldsymbol{r}_{FF})}{\boldsymbol{Gn}'(\boldsymbol{r}_i,\boldsymbol{r}')\boldsymbol{E}^i(\boldsymbol{r})}. \tag{21}$$

Then, the convolution kernel function can be written as

$$\boldsymbol{W}(\boldsymbol{r}_{FF}) = F[\omega_i.] \tag{22}$$

Finally, the substitution of Equation (22) into Equation (16) completes the transformation of the FF.

2.3. FF RCS Correction

In order to resolve the inconsistency between the results obtained from deriving FF RCS values from NF RCS measurements for targets with complex shapes and the results of directly measuring FF RCS, actual FF measurement data must be generated to correct the derived FF RCS value from the near-to-far field transformation. This section examines the FF scattering field data consisting of angle samples that are uniformly spaced in frequency. Each sample is represented as a sum of the product of a frequency-independent term and the complex sinusoids that correspond to scattering centers, which are known as the GTD scattering center model [16]. The measurements of the signal at these angles can be modeled as subject to white Gaussian measurement noise with zero means $\omega(\theta, \varphi, f)$.

$$\boldsymbol{E}s(\varphi,\theta,f) = \sum_{i=1}^{M}\beta_i\left(j\frac{f}{f_0}\right)^{\gamma}\exp(-j2k(x_i\cos\varphi\cos\theta + y_i\cos\varphi\sin\theta + z_i\sin\theta)) + \omega(\varphi,\theta,f) \tag{23}$$

where φ is the azimuth angle, θ is the elevation angle, γ is the scattering type, (x_i, y_i, z_i) is the FF range coordinate, β_i is the coefficient of the scattering, M denotes the number of scattering center, f_0 is the initial frequency, and $f = f_0 + \Delta f$ is the step frequency. Since the scattering center model is formulated in the frequency domain, it is transformed into the time domain [17] using IFT, i.e., $\boldsymbol{Es}(\boldsymbol{r}_{FF}) = F^{-1}(\boldsymbol{E}s(\theta,\varphi,f))$. Then, an equivalent relationship between the scattering center model and the near-to-far field transformation model can be established by

$$\begin{gathered} \boldsymbol{E}(\boldsymbol{r}_{FF}) \propto \boldsymbol{Es}(\boldsymbol{r}_{FF})\boldsymbol{b} \\ \boldsymbol{b} \in \mathbb{R}^{\mathrm{n}} \end{gathered} \tag{24}$$

where $\boldsymbol{b}$ is the correction coefficient vector. From a logical deduction standpoint, the theoretical support for further computations is provided by the establishment of the optimal prediction model, where $\boldsymbol{E}(\boldsymbol{r}_{FF})$ and $\boldsymbol{Es}(\boldsymbol{r}_{FF})$ exhibit a proportional relationship with a proportionality constant of 1, i.e., $\boldsymbol{E}(\boldsymbol{r}_{FF}) = \boldsymbol{Es}(\boldsymbol{r}_{FF})\boldsymbol{b}$.

By utilizing Equation (24), the model is transformed into a system identification problem where the input, output, and state of the system are defined to estimate the corresponding system parameters. If the system includes an internal variable $\boldsymbol{Es}(\boldsymbol{r}_{FF})$, which is a function of the system input $\boldsymbol{E}^i(\boldsymbol{r})$ or other variables $\boldsymbol{J}_s$, the system output $\boldsymbol{E}(\boldsymbol{r}_{FF})$ is a linear function of the internal variable $\boldsymbol{Es}(\boldsymbol{r}_{FF})$, as well as the azimuth angle parameter vector φ and the possible disturbance $\boldsymbol{v}(\boldsymbol{r}_{FF})$.

Next, a quadratic criterion function [18,19] is constructed to minimize the sum of squared errors, thereby transforming the problem into an optimization using the method of least squares, which leads to

$$J(\boldsymbol{b}) = \arg\min_{\boldsymbol{b}} \frac{1}{2} \|\boldsymbol{Es}(\boldsymbol{r}_{FF})\boldsymbol{b} - (\boldsymbol{E}(\boldsymbol{r}_{FF}) + \boldsymbol{v}(\boldsymbol{r}_{FF}))\|_2^2 \tag{25}$$

where $\boldsymbol{v}(\boldsymbol{r}_{FF})$ is the white Gaussian noise vector with zero mean. By taking the derivative of $\boldsymbol{b}$ and using NGS, the estimation value $\hat{b}(n)$ can be obtained as

$$\begin{gathered} \hat{b}(i+1) = \hat{b}(i) - \mu \cdot \nabla \left[J(\hat{b}(i)) \right] \\ i \in 1, 2, ..., n \end{gathered} \tag{26}$$

where $\hat{b}(i)$ is the i-th estimation component of $\boldsymbol{b}$, n denotes the length of vector, the value μ is a user-defined step size, and ∇ is gradient. Iterative computation, as specified by Formula (26), enables the calculation of the correction vector, which constitutes a crucial aspect proposed in this paper for addressing the issue of RCS error.

Since the calculation of the RCS in the FF is independent of distance, the iteratively computed parameters are substituted into Equation (24) to obtain the corresponding RCS value, represented by σ_{FF1} and σ_{FF2}, respectively.

$$\begin{aligned} \sigma_{FF1} &= 4\pi \frac{|\boldsymbol{Es}(\boldsymbol{r}_{FF})\boldsymbol{b}|^2}{\left|\boldsymbol{E}^i(\boldsymbol{r}_{FF})\right|^2} \\ \sigma_{FF2} &= 4\pi \frac{|\boldsymbol{E}(\boldsymbol{r}_{FF})|^2}{\left|\boldsymbol{E}^i(\boldsymbol{r})\right|^2} \end{aligned} \tag{27}$$

To visually demonstrate the theoretical impact of near-to-far field transformation and correction, Figure 4 presents a comparison of three point source RCS scenarios. The red RCS curve corresponds to the near-to-far field transformation, i.e., extrapolation. The green curve represents the RCS calculated using the GTD scattering center model based on the reference FF data. Finally, the blue curve represents the RCS that has been corrected using the proposed NGS iterative calculation method in this paper.

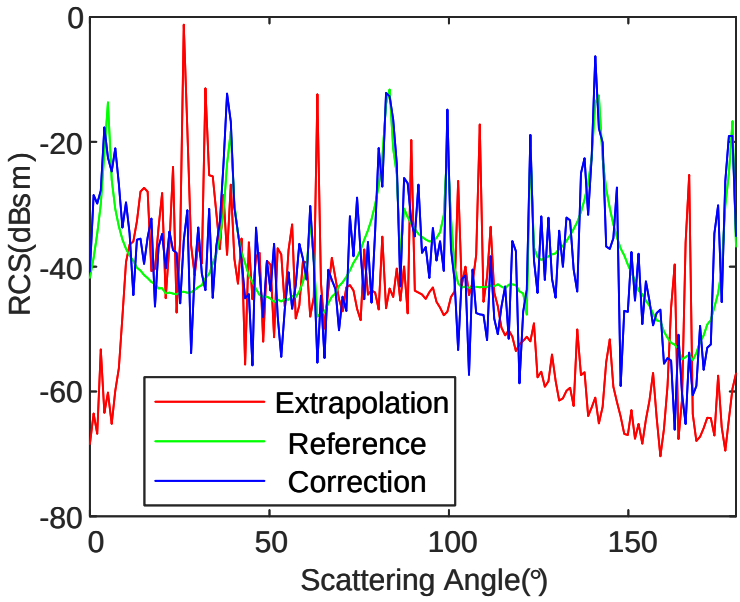

Figure 4. The comparison of FF RCS.

3. Experiments Results and Analysis Discussion

To demonstrate the effectiveness of the proposed method, we performed three experiments with an incident frequency of 2 GHz. In experiment 1, we obtained NF data from a small hexahedral target model, as shown in Figure 5, simulated by FEKO, transformed the NF E-field to the FF using the convolution kernel, and compared its RCS with FEKO's simulation of the FF RCS. Experiment 2 focused on calibrating the amplitude of the signal by employing NF measurements obtained from simulated test data. These measurements were utilized to derive a FF model, which was then compared against actual FF measurements to assess its accuracy. Finally, in Experiment 3, we utilized the GTD scattering center model to correct the RCS results of Experiment 2 based on FEKO's FF simulation data.

3.1. Experiment 1

As depicted in Figure 5, the geometry model was established by FEKO, and the necessary NF parameters were configured. Equation (15) defines the NF RCS by considering the denominator $\boldsymbol{E}^i(\boldsymbol{r})$ in the expression to represent the field strength of the antenna hood irradiated on the target surface. The model is sectioned based on the scanning plane where the monostatic RCS transmitter is located. During model processing, the incident direction of each angle of the model is determined, and the distance r from the point where the main lobe of the transmitting antenna first reaches the target to the origin of the coordinate system is calculated. On the other hand, the scattering field $\boldsymbol{E}^s(\boldsymbol{r}')$ to the target is denoted by $(\boldsymbol{r}')$.

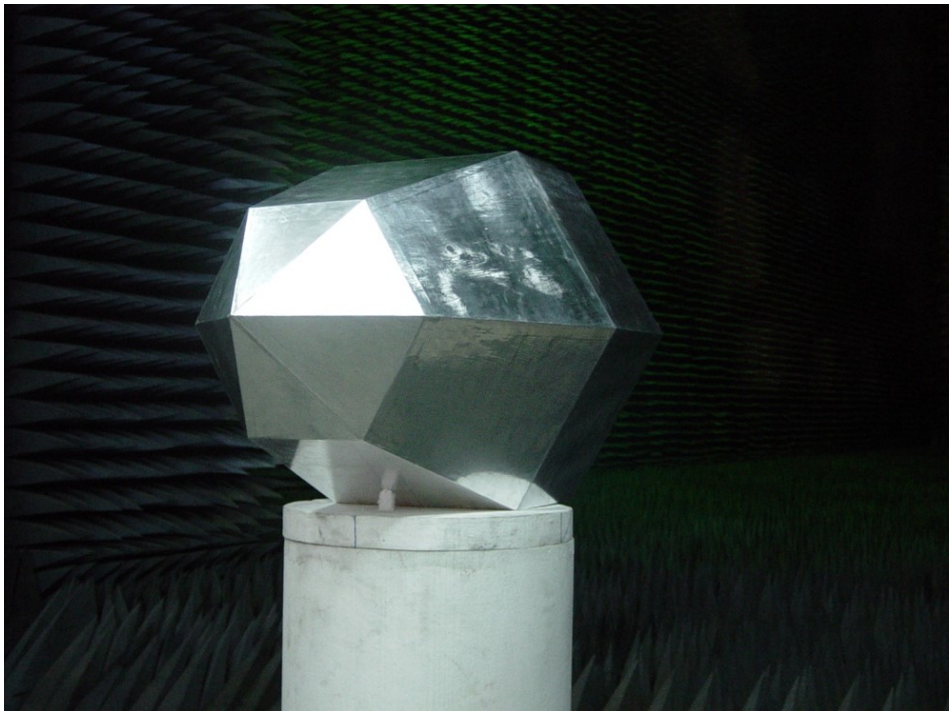

Figure 5. 1:1 model of a small hexahedral target mounted on a microwave darkroom turntable.

The experiment involved simulating the NF scattering E-field and RCS for four scattering distances using both HH and VV polarization modes. The four distances, NF1 to NF4, increase sequentially from short to long. Figures 6 and 7 illustrate the NF scattering E-field and RCS, respectively. The results show a decrease in E-field values and a corresponding change in RCS as the distance increases.

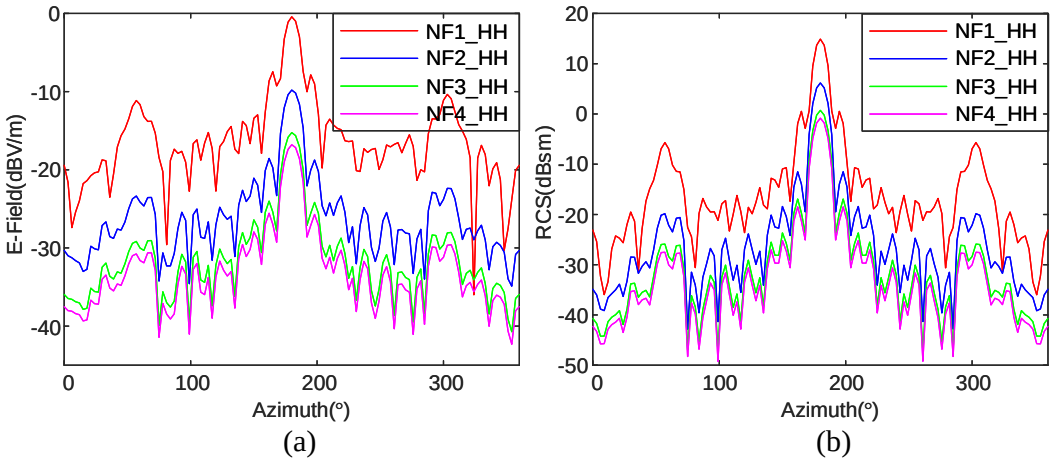

Figure 6. Four HH polarization modes at different distances from NF1 to NF4: (**a**) E-Field; (**b**) RCS.

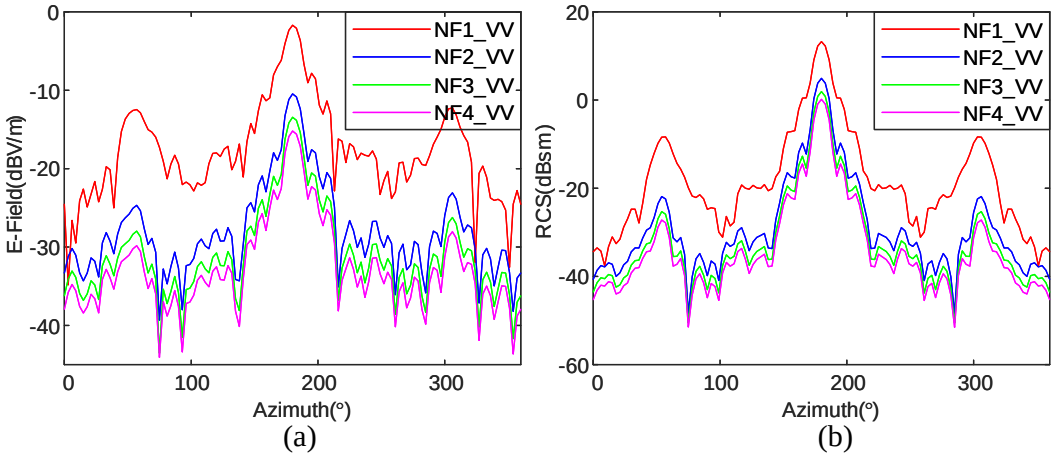

Figure 7. Four VV polarization modes at different distances from NF1 to NF4: (**a**) E-Field; (**b**) RCS.

According to the theory presented in Section 2, the near-to-far transformation kernel in Equation (22) is used to transform the NF E-field to the FF RCS. In this experiment, the FF input voltage $U_{in}(r_{FF})$ is approximated by the NF excitation voltage $U_{in}(r)$ and $\boldsymbol{E}^i(\boldsymbol{r})$ can be obtained by Equation (3). To obtain the kernel, the distance of the NF is substituted into the dyadic Green function in Equations (4) and (5) accordingly and then used FT to derive the kernel. Moreover, by substituting the near-to-far kernel into Equation (16), the FF RCS can be calculated as $\sigma_{FF} = 4\pi \frac{|\boldsymbol{E}(\boldsymbol{r}_{FF})|^2}{|\boldsymbol{E}^i(\boldsymbol{r})|^2}$.

Figures 8 and 9 illustrate the FF E-field and RCS, respectively. The black line in both figures represents the results of the near-to-far transformation, which shows better accuracy than the FF RCS, not only in the HH polarization mode but also in the VV mode. The NF E-field and RCS can be approximated to the FF RCS since the square of the NF distance is proportional to the NF scattering field.

Based on the figures presented in Figures 6–9, it can be concluded that as the distance between the target and the measurement device increases, the NF RCS becomes more similar to the FF RCS. This relationship is shown in Figure 10, where the NF distances are denoted as NF1, NF25, and NF50, with NF50 being longer than NF25 and NF25 being longer than NF1.

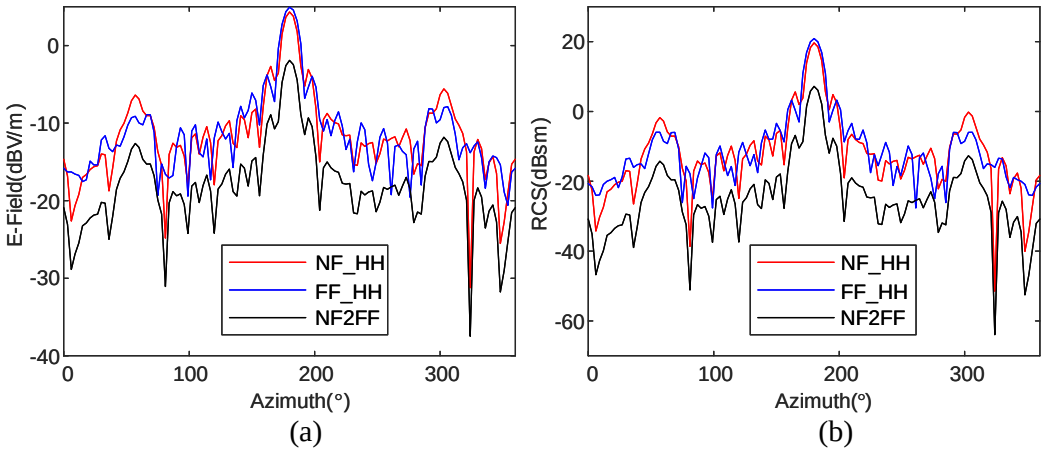

Figure 8. The comparison of NF E-Field and RCS in both HH polarization modes, the FF situation, and the proposed NFFFT calculation without amplitude correction: (**a**) E-Field; (**b**) RCS.

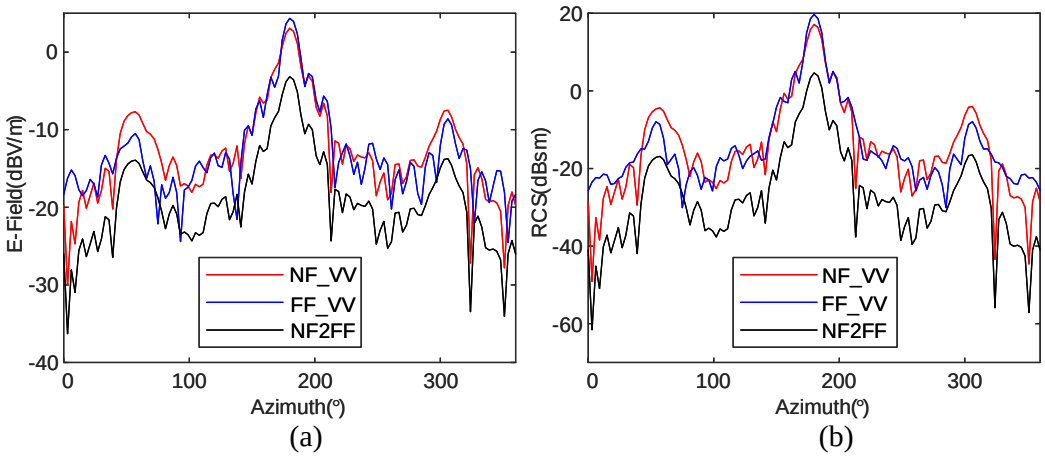

Figure 9. The comparison of NF E-Field and RCS in both VV polarization modes, the FF situation, and the proposed NFFFT calculation without amplitude correction: (**a**) E-Field; (**b**) RCS.

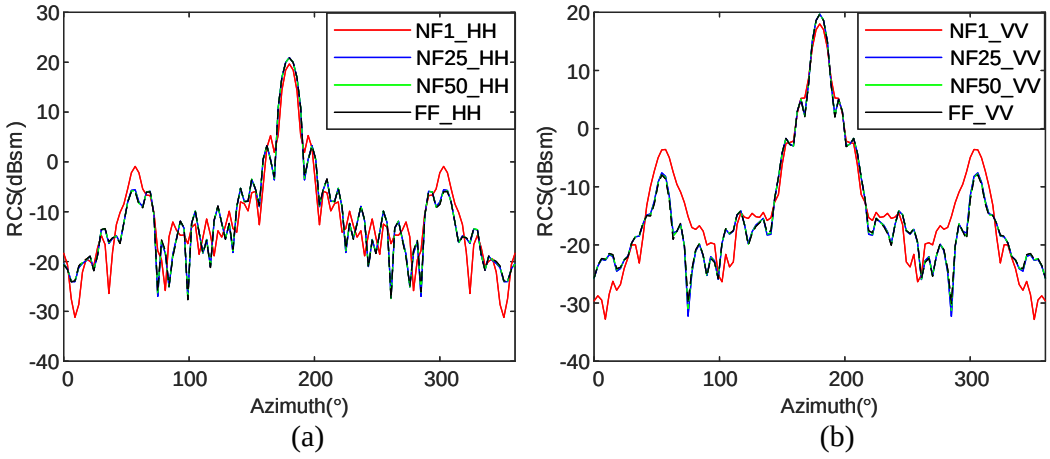

Figure 10. The comparison of NF E-Field and RCS in both HH and VV polarization modes for different distances with the FF situation: (**a**) HH polarization; (**b**) VV polarization.

3.2. Experiment 2

A function, in conjunction with the hexahedral target model, was utilized in this experiment to generate NF data that served as the actual measured value for accurately estimating the amplitude of the NF E-field. The Hankel function was then constructed using the NF scattering field and the corresponding distance. To simplify the calculation, the E-field was substituted for the voltage parameter in Equation (9). The numerator in the Hankel function was generated by FEKO, whereas the denominator represented the realistic measurement values. The amplitude was estimated accurately using the SSM method through the main SVD extraction. Furthermore, the estimated amplitude was substituted into the near-to-far transformation kernel, and the corrected FF E-field and RCS were compared with the original FF data. Additionally, the error of amplitude correction is calculated as

$$\boldsymbol{Err} = 10\log(|\sigma_{FF1} - \sigma_{FF2}|). \tag{28}$$

Figures 11 and 12 illustrate the FF E-field and RCS simulations for various polarization modes. The error curve, represented by the pink line in the figures, is computed using Equation (28). A notable correlation can be observed between the RCS derived from the near-to-far transformation and the amplitude correction line, as demonstrated by the figures. To verify the accuracy of the SSM method for amplitude estimation, error calculations were performed, which revealed that the results were consistent with the theoretical framework proposed in this study.

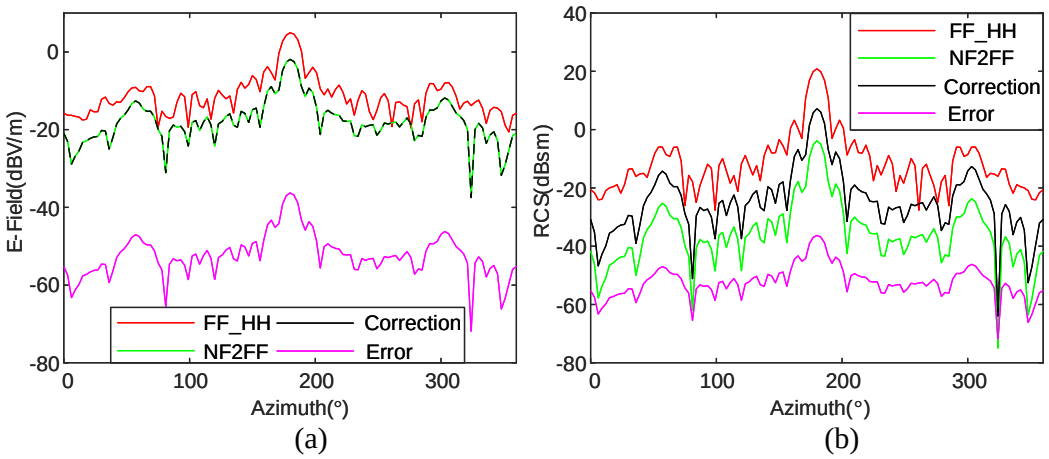

Figure 11. The comparison of FF E-Field and RCS between NFFFT and correction in HH polarization modes: (**a**) E-Field; (**b**) RCS.

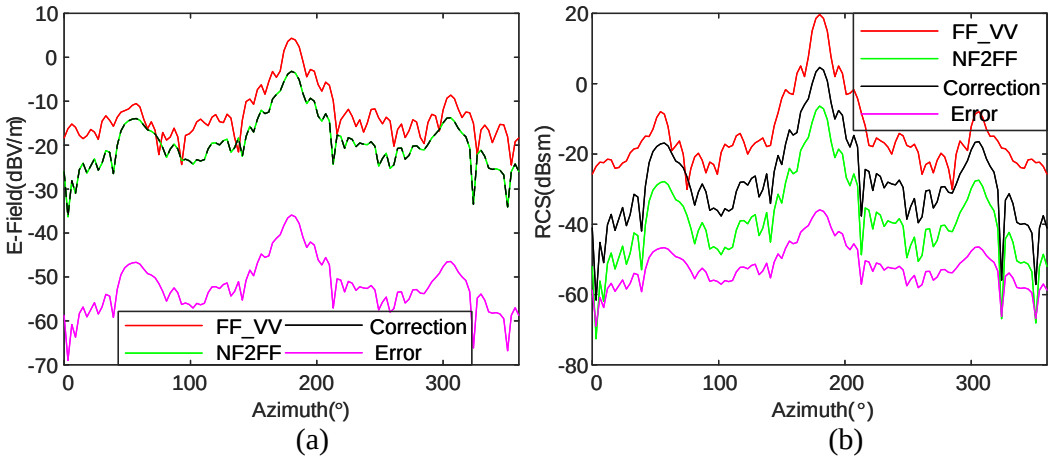

Figure 12. The comparison of NF E-Field and RCS between NFFFT and correction in VV polarization modes: (**a**) E-Field; (**b**) RCS.

3.3. Experiment 3

The focus of the aforementioned study was on the results of the NF simulation and transformation. Therefore, in this experiment, our aim was to compare FF simulation and correction. To model the FF signal, a scattering center model was utilized, which can be considered a realistic FF test signal. The same elevation and azimuth angles as in the FEKO simulation were set, and the initial frequency was 2 GHz. To observe the variation of RCS with azimuth, the step frequency was set to be the same as the initial frequency. Subsequently, a 3D geometry model of the hexahedral target was constructed, and the positions of 156 scattering centers were defined, as shown in Figure 13.

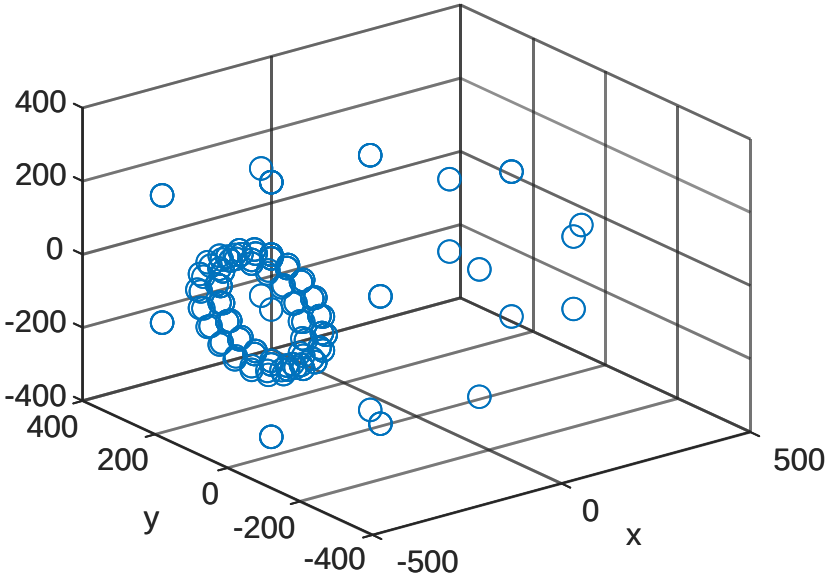

Figure 13. The scattering center points of the 3D geometry model corresponding to the hexahedral target.

According to the method proposed in [2], the RCS can be calculated using the complex scattering coefficient $\gamma(k_x, k_y)$ expressed as the reflectivity image $\psi(r_i, \theta, \varphi)$, which is obtained through the backward scattering distribution function represented by the GTD scattering center function in Equation (23). Therefore, a new formular can be derived to express the relationship between FF RCS $\boldsymbol{\sigma'}_{FF}$ and backward scattering function $\boldsymbol{E}s(\varphi, \theta, f)$, the discrete formulation can be expressed as

$$\boldsymbol{\sigma'}_{FF} = \left|\gamma(k_x, k_y)\right|^2 \tag{29}$$

$$\gamma(k_x, k_y) = \int_{-\infty}^{\infty}\int_{-\infty}^{\infty} \exp(j2\boldsymbol{k}\cdot\boldsymbol{r})\psi(\boldsymbol{r}_i, \varphi, \theta)dxdy \tag{30}$$

$$\psi(\boldsymbol{r}_i, \varphi, \theta) = \int_0^{\infty} IFFT[FFT[\boldsymbol{E}s(\varphi, \theta, f)] \cdot FFT[\xi(f, \boldsymbol{r}_i)]]fdf \tag{31}$$

where $\xi(f, \boldsymbol{r}_i) = e^{j4\pi(f/c)\|\boldsymbol{r}_{FF}-\boldsymbol{r}_i\|}\|\boldsymbol{r}_{FF} - \boldsymbol{r}_i\|^2$ is focusing operator [2]. Assuming a frequency center of 2 GHz and a frequency band of 4 GHz, Figure 14 shows the ISAR image of the hexahedral target model, which consists of 156 scattering centers.

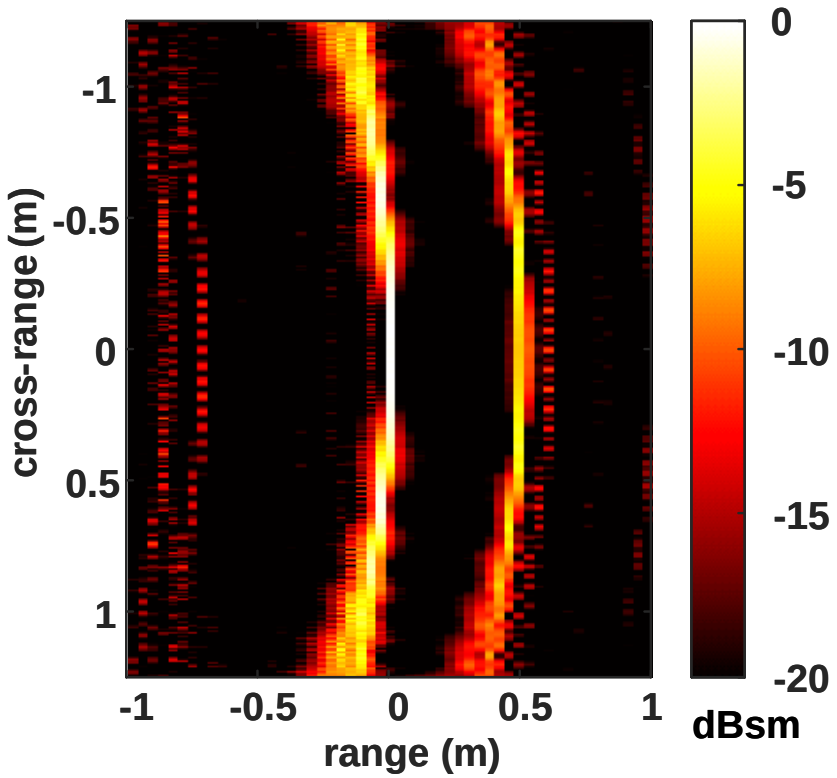

Figure 14. The ISAR image of the hexahedral target model consist of 156 scattering centers.

To compare the RCS obtained from the GTD scattering center model with the results obtained from the method of moment (MOM), Figure 15 presents the monostatic RCS obtained using different methods. The red and blue lines show the FF RCS computed by FEKO, whereas the green line shows the FF GTD scattering center RCS. From these results, it is evident that different calculation methods lead to different results. Thus, there is a need to analyze and correct the errors based on the complex EM environment.

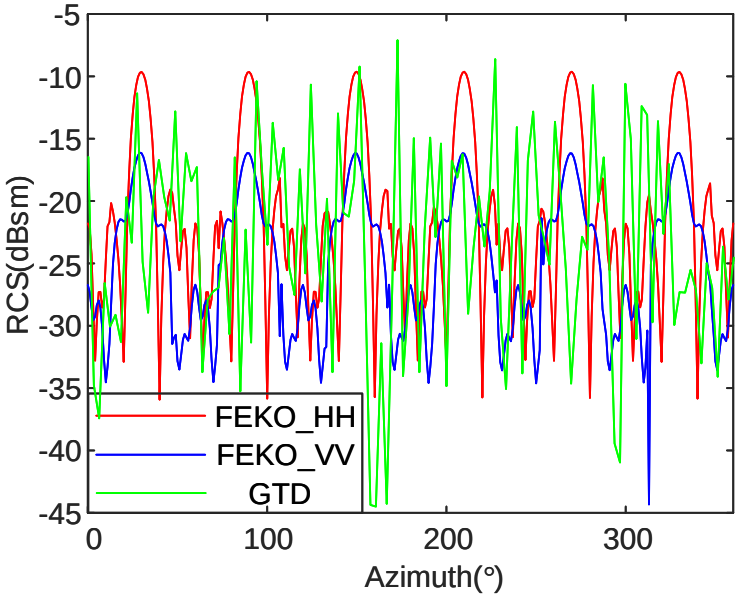

Figure 15. Monostatic FF RCS simulation.

The complexity of identification algorithms is an important criterion for evaluating their quality, and it is typically measured as the sum of the number of multiplication and addition operations required. In accordance with the approach outlined in Section 2.3, we employed NGS system identification to perform data correction. The algorithm steps are as follows.

Step 1: Define the termination accuracy requirement $\varepsilon > 0$, initialize the start iteration variable $num = 0$, and let the parameter of disturbance $\boldsymbol{v}(\boldsymbol{r}_{FF})$ be a random value.

Step 2: Calculate gradients $\left[J(\hat{b}(n))\right]$, if $\left\|J(\hat{b}(n))\right\| < \varepsilon$, go to the step 5 and output the approximate optimization solution $\hat{b}(n)$. Otherwise, go to step 3.

Step 3: Take the negative gradient $-\nabla\left[J(\hat{b}(n))\right]$ as the direction of descent and find the optimal step size μ by one-dimension search, which guarantees that the function value is minimized after moving in the corresponding direction by $\mu = \arg\min_{\mu \geq 0} J(\boldsymbol{b})$.

Step 4: Iterative variable, return to step 2 for a loop.

Step 5: Final.

The monostatic FF RCS obtained by FEKO and the GTD scattering center model are presented in Figure 16. The red line represents the result obtained from FEKO simulations, the blue line corresponds to the outcome generated using 156 scattering centers, and the green line is the result corrected using the NGS method proposed in this study. It is evident from the figure that the corrected RCS shows good results under uncertainty test conditions.

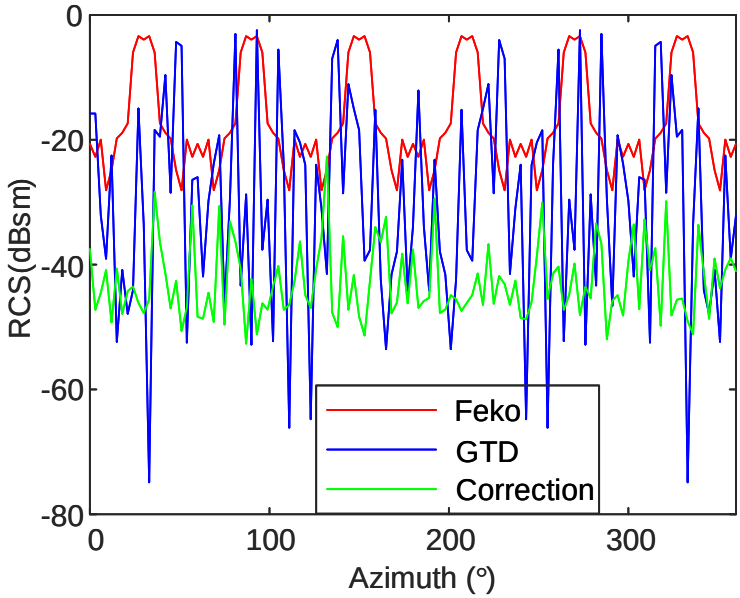

Figure 16. The comparison of monostatic FF RCS.

4. Conclusions

This paper proposes four contributions to the near-to-far transformation process. Firstly, the use of the SSM to perform amplitude estimation effectively corrects the strength for near-to-far transformation by accounting for errors between the theoretical NF E-field and realistic measurement. Next, a near-to-far transformation kernel was derived, which effectively solves the FF RCS calculation. Subsequently, the equation for transforming NF to FF was derived, addressing the problem of computing FF RCS from the NF. Finally, the NGS system identification method is utilized to correct the FF RCS error between the GTD scattering center model and the reference FF RCS computed by FEKO. These contributions are highly relevant in the creation of sophisticated measurement systems that demand highly adaptable transformation algorithms. The simulation-based experiments conducted in this paper provide further evidence of the efficacy of these techniques in improving near-to-far transformation accuracy.

Author Contributions: Conceptualization, J.Z.; methodology, J.H.; software, J.H.; validation, J.H. and Y.D.; investigation, Y.D.; writing—original draft preparation, J.H.; writing—review and editing, J.H. and J.Z. All authors have read and agreed to the published version of the manuscript.

Funding: This work was funded in part by the National Natural Science Foundation of China (Grant No. 61671239, No. 61801212), in part by the Key Laboratory of Radar Imaging and Microwave Photonics (Nanjing Univ. Aeronaut. Astronaut.), the Ministry of Education, the Nanjing University of Aeronautics and Astronautics, Nanjing, 210016, China, in part by Innovation experiment competition cultivation (SAR image analysis system based on FPGA) (Nanjing Univ. Aeronaut. Astronaut.), in part by the Basic Ability Improvement Research Project of Young and Middle-aged College Teachers in Guangxi (2020KY570012).

Institutional Review Board Statement: Not applicable.

Informed Consent Statement: Not applicable.

Data Availability Statement: The study did not report any data.

Conflicts of Interest: The authors declare no conflict of interest.

References

1. Schnattinger, G.; Mauermayer, R.A.; Eibert, T.F. Monostatic radar cross section near-field far-field transformations by multilevel plane-wave decomposition. *IEEE Trans. Antennas Propag.* **2014**, *62*, 4259–4268. [CrossRef]
2. Vaupel, T.; Eibert, T.F. Comparison and application of near-field ISAR imaging techniques for far-field radar cross section determination. *IEEE Trans. Antennas Propag.* **2006**, *54*, 144–151. [CrossRef]
3. Francis, M. IEEE recommended practice for near-field antenna measurements. *IEEE Standard* **2012**, *1720* , 5–6.
4. Qureshi, M.A.; Schmidt, C.H.; Eibert, T.F. Near-field error analysis for arbitrary scanning grids using fast irregular antenna field transformation algorithm. *Prog. Electromagn. Res. B* **2013**, *48*, 197–220. [CrossRef]
5. Schmidt, C.H.; Eibert, T.F. Multilevel plane wave based near-field far-field transformation for electrically large antennas in free-space or above material halfspace. *IEEE Trans. Antennas Propag.* **2009**, *57*, 1382–1390. [CrossRef]
6. Li, J.; Wang, X.; Wang, T. On the validity of Born approximation. *Prog. Electromagn. Res.* **2010**, *107*, 219–237. [CrossRef]
7. Naishadham, K.; Piou, J.E. A robust state space model for the characterization of extended returns in radar target signatures. *IEEE Trans. Antennas Propag.* **2008**, *56*, 1742–1751. [CrossRef]
8. Viberg, M. Subspace-based methods for the identification of linear time-invariant systems. *Automatica* **1995**, *31*, 1835–1851. [CrossRef]
9. Kung, S.Y.; Arun, K.S.; Rao, D.B. State-space and singular-value decomposition-based approximation methods for the harmonic retrieval problem. *JOSA* **1983**, *73*, 1799–1811. [CrossRef]
10. Tripathy, P.; Srivastava, S.; Singh, S. A modified TLS-ESPRIT-based method for low-frequency mode identification in power systems utilizing synchrophasor measurements. *IEEE Trans. Power Syst.* **2010**, *26*, 719–727. [CrossRef]
11. Iordache, M.D.; Bioucas-Dias, J.M.; Plaza, A.; Somers, B. MUSIC-CSR: Hyperspectral unmixing via multiple signal classification and collaborative sparse regression. *IEEE Trans. Geosci. Remote Sens.* **2013**, *52*, 4364–4382. [CrossRef]
12. Potter, L.C.; Chiang, D.M.; Carriere, R.; Gerry, M.J. A GTD-based parametric model for radar scattering. *IEEE Trans. Antennas Propag.* **1995**, *43*, 1058–1067. [CrossRef]
13. Huang, J.; Liu, X.; Zhou, J.; Deng, Y. RCS diagnostic imaging using parameter extraction technique of state space method. *Radio Sci.* **2023**, *58*, e2022RS007565. [CrossRef]
14. Knott, E.F. A progression of high-frequency RCS prediction techniques. *Proc. IEEE* **1985**, *73*, 252–264. [CrossRef]
15. Hu, C.; Li, N.; Chen, W.; Guo, S. A near-field to far-field RCS measurement method for multiple-scattering target. *IEEE Trans. Instrum. Meas.* **2018**, *68*, 3733–3739. [CrossRef]
16. Zhou, J.; Zhao, H.; Shi, Z.; Fu, Q. Global scattering center model extraction of radar targets based on wideband measurements. *IEEE Trans. Antennas Propag.* **2008**, *56*, 2051–2060. [CrossRef]
17. Bunger, R. Time-Domain Evaluation of Full-Wave Scattering Center Models. *IEEE Antennas Wirel. Propag. Lett.* **2020**, *19*, 912–915. [CrossRef]
18. Bao, B.; Xu, Y.; Sheng, J.; Ding, R. Least squares based iterative parameter estimation algorithm for multivariable controlled ARMA system modelling with finite measurement data. *Math. Comput. Model.* **2011**, *53*, 1664–1669. [CrossRef]
19. Ma, H.; Zhang, X.; Liu, Q.; Ding, F.; Jin, X.B.; Alsaedi, A.; Hayat, T. Partially-coupled gradient-based iterative algorithms for multivariable output-error-like systems with autoregressive moving average noises. *IET Control. Theory Appl.* **2020**, *14*, 2613–2627. [CrossRef]